REPORT DOCUMENTATION PAGE

Form Approved
OMB No. 0704-0188

1. REPORT DATE *(DD-MM-YYYY)*	**2. REPORT TYPE**	**3. DATES COVERED** *(From - To)*
Jan 2014	Technical Paper	Jan 2014-Jan 2015

4. TITLE AND SUBTITLE
Study of Liquid Breakup Process in Solid Rocket Motors

5a. CONTRACT NUMBER
In-House

5b. GRANT NUMBER

5c. PROGRAM ELEMENT NUMBER

6. AUTHOR(S)
Ryo Amano, Y-H Yen, Timothy Miller, Venke Sankaran, Adam Ebnit, Malissa Lightfoot

5d. PROJECT NUMBER

5e. TASK NUMBER

5f. WORK UNIT NUMBER
Q16H

7. PERFORMING ORGANIZATION NAME(S) AND ADDRESS(ES)

Air Force Research Laboratory (AFMC)
AFRL/RQRP
10 E. Saturn Blvd.
Edwards AFB, CA, 93524-7680

8. PERFORMING ORGANIZATION REPORT NO.

9. SPONSORING / MONITORING AGENCY NAME(S) AND ADDRESS(ES)

Air Force Research Laboratory (AFMC)
AFRL/RQR
5 Pollux Dr.
Edwards AFB, CA, 93524-7048

10. SPONSOR/MONITOR'S ACRONYM(S)

11. SPONSOR/MONITOR'S REPORT NUMBER(S)
AFRL-RQ-ED-TP-2014-007

12. DISTRIBUTION / AVAILABILITY STATEMENT
Approved for public release; distribution unlimited

13. SUPPLEMENTARY NOTES
Technical Paper presented at AIAA SciTech 2015, Kissimmee, Florida, 5-9 Jan 2015.
PA#14081

14. ABSTRACT

In a solid rocket motor (SRM), when the propellant combusts, the aluminum is oxidized into alumina (Al_2O_3) which, under the right flow conditions, tends to agglomerate into molten droplets, impinge on the chamber walls, and then flow along the nozzle wall. Such agglomerates can cause erosive damage. The focus of the current research is to characterize the agglomerate flow within the nozzle section by studying the breakup process of a liquid film that flows along the wall of a straight channel while a high-speed gas moves over it. We have used an unsteady-flow Reynolds-Averaged Navier-Stokes code (URANS) to investigate the interaction of the liquid film flow with the gas flow, and analyzed the breakup process for different flow conditions. The rate of the wave breakup was characterized by introducing a breakup-length-scale for various flow conditions based on the Volume Fraction (VF) of the liquid, which is an indicator of a two-phase flow liquid breakup level. A smaller breakup-length-scale means that smaller drops have been created during the breakup process. The study covers the breakup and fluid behaviors based on different gas-liquid momentum flux ratios, different surface tension and viscosity settings, different Ohnesorge numbers (Oh), and different Weber numbers. Both water and molten aluminum flows were considered in the simulation studies. The analysis demonstrates an effective method of correlating the liquid breakup with the main flow conditions in the nozzle channel path.

15. SUBJECT TERMS

16. SECURITY CLASSIFICATION OF:			**17. LIMITATION OF ABSTRACT**	**18. NUMBER OF PAGES**	**19a. NAME OF RESPONSIBLE PERSON**
					Timothy Miller
a. REPORT	**b. ABSTRACT**	**c. THIS PAGE**			**19b. TELEPHONE NO** *(include area code)*
Unclassified	**Unclassified**	**Unclassified**	SAR	20	661-525-5323

Standard Form 298 (Rev. 8-98)
Prescribed by ANSI Std. 239.18

Study of Liquid Breakup Processes in Solid Rocket Motors

R.S. Amano[a], Yi-Hsin Yen[b]

University of Wisconsin Milwaukee, Milwaukee WI, 53211

Timothy C. Miller, Adam Ebnit, Malissa Lightfoot and Venke Sankaran

Air Force Research Laboratory, Edwards, CA

Abstract

In a solid rocket motor (SRM), when the propellant combusts, the aluminum is oxidized into alumina (Al_2O_3) which, under the right flow conditions, tends to agglomerate into molten droplets, impinge on the chamber walls, and then flow along the nozzle wall. Such agglomerates can cause erosive damage. The focus of the current research is to characterize the agglomerate flow within the nozzle section by studying the breakup process of a liquid film that flows along the wall of a straight channel while a high-speed gas moves over it. We have used an unsteady-flow Reynolds-Averaged Navier-Stokes code (URANS) to investigate the interaction of the liquid film flow with the gas flow, and analyzed the breakup process for different flow conditions. The rate of the wave breakup was characterized by introducing a breakup-length-scale for various flow conditions based on the Volume Fraction (VF) of the liquid, which is an indicator of a two-phase flow liquid breakup level. A smaller breakup-length-scale means that smaller drops have been created during the breakup process. The study covers the breakup and fluid behaviors based on different gas-liquid momentum flux ratios, different surface tension and viscosity settings, different Ohnesorge numbers (Oh), and different Weber numbers. Both water and molten aluminum flows were considered in the simulation studies. The analysis demonstrates an effective method of correlating the liquid breakup with the main flow conditions in the nozzle channel path.

Nomenclature

g	=	gravity
K	=	temperature in Kelvin
L	=	characteristic length of the droplet
P	=	pressure
T	=	temperature
t	=	time
$\overline{u'}$	=	time averaged fluctuating velocity component in Reynolds Stress Model
v, V	=	general velocity expression
Oh	=	Ohnesorge numbers $\equiv Oh = \sqrt{We} / Re$
Re	=	Reynolds number $\equiv Re = \rho v L / \mu$
We	=	Weber number $\equiv We = (\rho v^2 L) / \sigma$

Symbol

α	=	alumina temperature correlated density parameter
β	=	thermal expansion coefficient
θ	=	temperature in Reynolds Stress Model
μ	=	viscosity
ρ	=	density of fluid
σ	=	surface tension
Ω	=	angular velocity

I Introduction

[a] Professor, Mechanical Engineering, 115 E. Reindl Way, Glendale WI,53212, Associate Fellow of AIAA

[b] Graduate Student, Mechanical Engineering, 115 E. Reindl Way, Glendale WI,53212, Student Member of AIAA

TYPICALLY solid rocket motors (SRM) use an aluminum-based propellant[1] due to its high energy density per unit volume[2]. However, aluminum propellant has some performance issues after it has been burned. During the propellant combustion, the aluminum particles oxidize into alumina (Al_2O_3) particles and flow from the combustion chamber to the nozzle as a liquid. The chemical and mechanical erosion caused by the alumina particles is a particular problem to be avoided in a SRM because of the effects on ballistic performance[3]. Most of the erosion takes place near the nozzle throat, changing the nozzle throat geometry. It is considered excessive (from a design perspective) for most SRM throats to experience more than a 5% change in cross-sectional area, because any larger change would result in an unacceptable drop in the velocity of the exhaust gas[4]. The velocity contours of the solid rocket flowfield are affected by the multiphase particle motion inside the combustion chamber; which further limits the performance, according to a study by Nayfeh and Saric[5]. Moreover, because of the geometry of the motor, molten alumina agglomerates can form, resulting in two-phase flow losses[6,7,8]. These agglomerates lower the propulsive efficiency of the exhaust flow because the agglomerates do not expand in the nozzle and also create a drag force on the flow[9,10]. Depending on the alumina particle size and the alumina particle-gas mixture percentage, two-phase flow losses can reduce the propellant specific impulse by as much as 6%[11,12]. The operating environment of the combustion chamber of an SRM is extremely severe, with temperatures reaching 3,000K to 3,500K and pressure over 2.0 x 10^7 Pa; alumina has an observed melting temperature of 2,327K and an evaporation temperature of about 3,200K at an atmospheric condition. Thus, the alumina exists as mostly liquid in the combustion chamber and in the nozzle, with some evaporation possibly occurring. Sometimes the alumina film becomes re-entrained near the nozzle throat and impinges on the diverging section of the rocket nozzle, causing erosive damage. Because of these effects, a better understanding of the phenomena is necessary for designing an SRM.

In gas-liquid two-phase flows, liquid droplet breakup behavior can be observed. Hinze[13,14] proposed using non-dimensional quantities such as the Weber number to characterize the breakup process. Large droplets have relatively large cross-sectional areas that lead to aerodynamic forces acting on them that are higher than the weaker surface tension that is attempting to hold the droplet in shape, so a higher Weber number for a droplet indicates a higher likelihood of breakup. The liquid alumina breakup mechanism in an SRM is more complicated than the breakup of droplets. The liquid alumina accumulates and attaches on the wall of the de Laval nozzle, forming a liquid film[15] that is shear driven and interacts with the surrounding air. The liquid film forms waves due to the shear, and breakup occurs at the crests of the waves. The breakup level increases with the surrounding gas velocity; more liquid breakup in the nozzle throat reduces the liquid alumina droplet size, resulting in easier discharge of droplets by the carrier gas instead of the alumina adhering to the nozzle wall.

In this study, an unsteady two-phase flow and a liquid breakup phenomenon are investigated by using a computer simulation model in a straight channel for different gas-liquid flow conditions to understand the interaction between the alumina flow and the high-speed gas flow. The results provide a better understanding of the alumina breakup phenomenon in an SRM.

Physical Parameters

In this study, three dimensionless numbers, Oh, We, and Re, have been applied to describe the flow field status. The Oh number describes the ratio of the viscous force to the inertial and surface tension forces. Theoretically, a large Oh number indicates a greater influence of viscosity that is a less active cause of breakup. The Oh number is defined as the following:

$$\mathrm{Oh} = \frac{\sqrt{\mathrm{We}}}{\mathrm{Re}} = \frac{\sqrt{\rho \mathrm{V}^2 L/\sigma}}{\rho \mathrm{V} L/\mu} = \frac{\mu}{\sqrt{\rho \sigma \mathrm{L}}} \qquad (1)$$

The Weber number also is often used in analyzing multiphase flow because it describes the ratio between the inertial force and the surface tension. When the Weber number is large, the surface tension is dominated by the deforming inertial forces, which leads to an easier liquid breakup process. The Weber number is defined in equation (2)

$$\mathrm{We} = \frac{\rho \mathrm{v}^2 L}{\sigma} \qquad (2)$$

where μ, ρ, and σ from the above equations are the viscosity, density, and surface tension, respectively, of the liquid, L is the characteristic length of the droplet; and v is the velocity of the carrier gas. The Reynolds number is also an

important reference dimensionless quantity that is defined as Re= ρvL/μ. However, the Reynolds number enters through the definition of the Oh number, and does not the directly affect the breakup phenomena.

Physical Models

For this simulation study, STAR-CCM+ was used to predict the flows by solving the unsteady Reynolds-Averaged Navier-Stokes (URANS) equations[16]. The system of equations was solved in an Eulerian multi-phase state with an implicit unsteady solver applying the volume of fluid (VOF) approach[17] for the interface between the liquid and gaseous phases.

The two-dimensional incompressible Reynolds-averaged Navier-Stokes equation coupled with the Volume of Fraction (VOF) model were used in this two-phase flow study. The Reynolds stress model (RSM) was applied to the simulation. The Reynolds stresses $\rho\overline{u_i'u_j'}$, can be expressed as the following[18].

$$\frac{\partial}{\partial t}(\rho\overline{u_i'u_j'}) + \frac{\partial}{\partial x_k}(\rho u_k\overline{u_i'u_j'}) = -\frac{\partial}{\partial x_k}[\rho\overline{u_i'u_j'u_k'} + \overline{p(\delta_{kj}u_i' + \delta_{ik}u_j')}] + \frac{\partial}{\partial x_k}[\mu\frac{\partial}{\partial x_k}(\overline{u_i'u_j'})] - \rho(\overline{u_i'u_k'}\frac{\partial u_j}{\partial x_k} + \overline{u_j'u_k'}\frac{\partial u_i}{\partial x_k}) - \rho\beta(g_i\overline{u_j'\theta} + g_j\overline{u_i'\theta}) + \overline{P(\frac{\partial u_i'}{\partial x_j} + \frac{\partial u_j'}{\partial x_i})} - 2\mu\overline{\frac{\partial u_i'}{\partial x_k}\frac{\partial u_j'}{\partial x_k}} - 2\rho\Omega_k(\overline{u_j'u_m'}\epsilon_{ikm} + \overline{u_i'u_m'}\epsilon_{jkm}) \quad (3)$$

In equation (3), the first term $\frac{\partial}{\partial t}(\rho\overline{u_i'u_j'})$ is the local time derivative term with ρ as the density and $\bar{u}'$ as the time averaged fluctuating velocity component, the second term $\frac{\partial}{\partial x_k}(\rho u_k\overline{u_i'u_j'})$ is the convection term, the third term $-\frac{\partial}{\partial x_k}[\rho\overline{u_i'u_j'u_k'} + \overline{p(\delta_{kj}u_i' + \delta_{ik}u_j')}]$ is the turbulent diffusion term, the fourth term $\frac{\partial}{\partial x_k}[\mu\frac{\partial}{\partial x_k}(\overline{u_i'u_j'})]$ is the molecular diffusion term with μ as the viscosity of fluid; the fifth term $\rho(\overline{u_i'u_k'}\frac{\partial u_j}{\partial x_k} + \overline{u_j'u_k'}\frac{\partial u_i}{\partial x_k})$ is the stress production term, the sixth term $\rho\beta(g_i\overline{u_j'\theta} + g_j\overline{u_i'\theta})$ is the buoyancy term with β as the thermal expansion coefficient, g as the acceleration direction, and θ as the temperature, the seventh term $\overline{P(\frac{\partial u_i'}{\partial x_j} + \frac{\partial u_j'}{\partial x_i})}$ is the pressure strain term, the eighth term $2\mu\overline{\frac{\partial u_i'}{\partial x_k}\frac{\partial u_j'}{\partial x_k}}$ is the dissipation term, and the ninth term $2\rho\Omega_k(\overline{u_j'u_m'}\epsilon_{ikm} + \overline{u_i'u_m'}\epsilon_{jkm})$ is the production by system rotation term with Ω as angular velocity.

Geometric Configuration

A rectangular channel, as shown in Figure 1, was considered for the present study. The channel has a 0.2 m inlet, where a 30 mm thick layer of liquid flows through the lower inlet section and air flows through the remaining upper inlet section. At a location 0.159 m from the inlet, a ramp with a height of 15 mm and an angle of 20 degrees is placed to create a flow separation. The total length of the channel is 1 m. Both the top and the right side of the boundaries are set as an open boundary.

The momentum flux ratio (MFR) is defined as:

$$\mathrm{MFR} = \frac{(\rho V^2)_{\mathrm{air}}}{(\rho V^2)_{\mathrm{liquid}}} \quad (4)$$

where ρ and V are the density and velocity properties of the fluid for air and the liquid phase in terms of the subscripts.

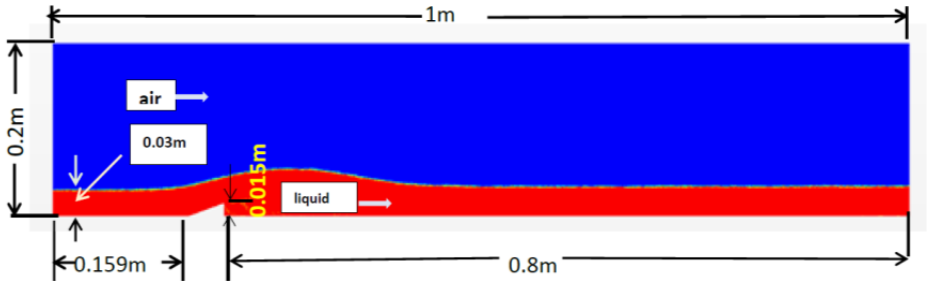

Figure 1: Flow geometry.

Properties of Fluids

In order to compare the liquid breakup behavior, the liquid properties such as viscosity and surface tension are tested for both alumina and water. The properties of liquids that have been applied to this simulation are shown in Table 1, where water is in a standard room temperature condition and the alumina is in a molten condition with a temperature of 3,000K. The high temperature viscosity and the surface tension are those proposed by Young[19], Blomquist,[20] and Glorieux[21] with a value of 0.046Pa-s for viscosity and 0.67N/m for surface tension. The density of alumina under high temperature is expressed by Glorieux[22] as shown below.

$$\rho = (2.79)[1 - \alpha(T - 2500)]g \cdot \mathrm{cm}^{-3} \quad (5)$$

Where $\alpha = 4.22 \times 10^{-5}\ K^{-1}$ and T is the temperature in Kelvin.

The reason to use water as one of the working fluids is that water can be more readily used for validation experiments. We also simulated different test liquids with different physics property combinations such as the viscosity and the surface tension, which are correlated with different liquid breakup behaviors when compared with alumina.

Table 1: Properties of Liquids

Materials	Density (kg/m3)	Viscosity (Pa-s)	Surface Tension (N/m)	Meting Point (K)	Vaporization Point (K)
$\mathrm{Alumina}_{3,000K}$	2,731	4.60E-02	0.67	2327	3200
Water	998	8.90E-04	0.074	273	373
Air	1.2	1.80E-05	NA	NA	NA

Boundary Length Definition

The boundary length is an important indicator in water breakup studies since it can be used to define the breakup characteristics. In order to demonstrate how this parameter is calculated in the present work, we use a test simulation as shown in Figure 2, where the computational domain dimensions are 1.0 m in length and 0.2 m in height, and the water and air are still and controlled only by gravity. The values of the VF of water and air are equal to 1 and 0, respectively. The cells with any values of VF between 1 and 0 will be the cells representing the phase boundary. The boundary length from this simulation setup is initially 1 m long.

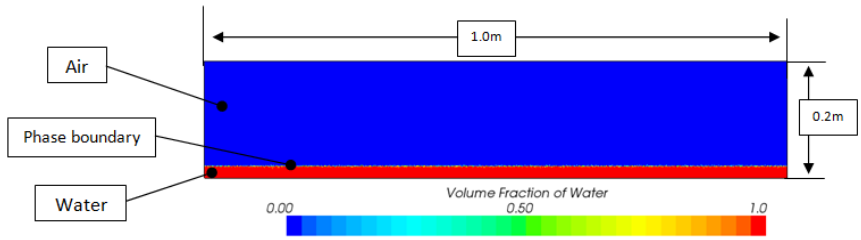

Figure 2 Phase boundary of two-phase fluid in computational domain

Once the test simulation is run, we determine the phase boundary length by counting how many cells are in the computational domain with the range of $0 < VF < 1$. The close-up view of the cells' boundary VF value is shown in Figure 3. Once we know the number of boundary cells and the size of the cells, we can calculate the boundary length.

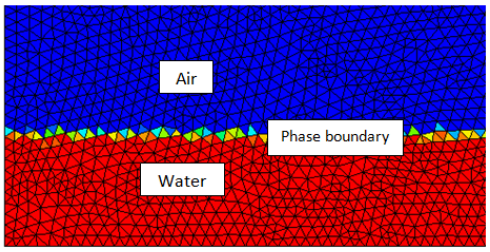

Figure 3 Close-up views of cells of phase boundary

Figure 4 shows the results from setting a target VF value ranging between 0.089 and 0.910. These values were chosen by adjusting the window so that the target boundary length of 1 m was approximated. The total number of cells with a value in the boundary VF range is 676 out of 104,500 cells in the entire computational domain. The averaged triangle cell area is 1.9×10^{-6} m^2 with a corresponding triangle altitude (height) of 1.49×10^{-3}m; therefore, based on the information above, we can get the result of the two-phase boundary length of 1.007m.

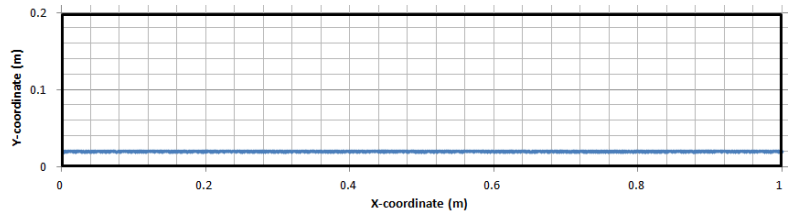

Figure 4 Data extracted from the computational domain for $0.089 < VF < 0.910$

Breakup Characteristic Length Definition

The boundary length provides a way to quantify the breakup level. Droplets are created from disturbances on the surface of the liquid. So, if there is no breakup, the two-phase boundary behaves relatively calmly, and results in a relatively straight or a gently wave-like surface with few droplets. Therefore, there is a relatively short boundary length as shown in Figure 5(a). On the other hand, if there is substantial liquid breakup occurring, then the surface behaves quite dynamically, with a very wavy surface and many droplets, resulting in a longer boundary length as shown in Figure 5(b).

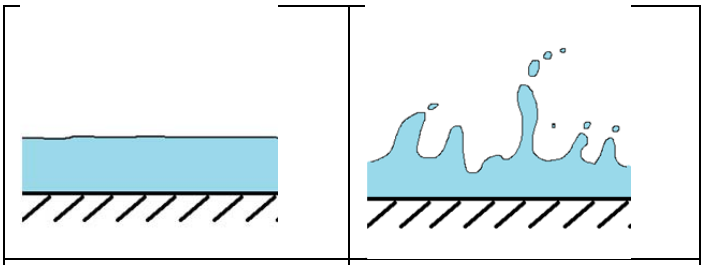

(a) No breakup, (b) Fractional breakup,

Figure 5 Wave breakup level

The higher the breakup level for the liquid, the longer the two-phase boundary will be; therefore, the boundary length is a good indicator for us to study the breakup level of a two-phase flow. However, the boundary length only signifies how long the boundary is instead of an average liquid droplet size. Therefore, the breakup characteristic length is introduced to define the average size of the separated liquid body. The breakup characteristic length is defined as:

$$\text{breakup characteristic length} = \frac{\text{liquid area}}{\text{boundary length}} \text{ (for 2-D)} \quad (6)$$

$$\text{breakup characteristic length} = \frac{\text{liquid volume}}{\text{boundary area}} \text{ (for 3-D)} \quad (7)$$

We can indirectly interpret that a larger breakup characteristic length corresponds to a smaller liquid breakup size. Figure 6 compares simulation results of alumina flows with MFR=0.015 (Figure 6, a.1) and MFR=0.15 (Figure 6, b.1). The blue lines for the VF between 0.089 and 0.910 represent the outline (boundary length) of the alumina, which were evaluated as 2.087m (Figure 6, a.2) and 6.676m (Figure 6, b.2). Similarly, the areas were computed as $0.0387m^2$ and $0.0316m^2$ for MFR=0.015 and MFR=0.15, respectively. Accordingly, the breakup characteristic lengths were 1.85cm and 0.47cm for MFR=0.015 and 0.15 respectively, with the higher value indicating less breakup and the lower value indicating more breakup.

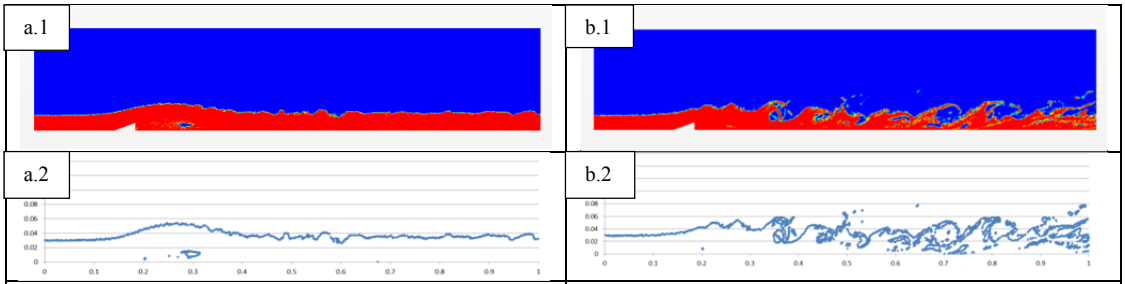

Boundary Length : 2.087 m Liquid Area: 0.0387 m2 Breakup Characteristic Length = 1.85 cm	Boundary Length : 6.676m Liquid Area: 0.0316 m2 Breakup Characteristic Length = 0.47 cm
MFR=0.015	MFR=0.15

Figure 6: Breakup shape for different alumina flows.

II RESULTS

Grid Independence Study

Four mesh sizes with computational domain cells numbering 100,000, 300,000, 500,000 and 1,000,000, are used to test the grid resolution, the boundary length, and the breakup phenomenon. The simulations apply to air and water as the two-phase media. The reason to use water is that it is more likely to breakup than alumina due to its lower surface tension, density, and viscosity, which would help us to capture the fluid breakup details for all four different mesh size settings. The velocity settings of these grid-independence study simulations are 26m/s and 5m/s, for the air and water respectively. Figure 7 (a) and (b) show the comparison of domain cell numbers between 100,000 and

1,000,000. Figure 7 (c) and (d) show the correlation between the mesh size and the boundary line for the cases of 100,000 cells and 1,000,000 cells. When the mesh is finer, the resolution of the mesh is better able to display two-phase boundary details; a longer boundary length is the result. However, if the mesh size is smaller than the detailed wave size, which means that the mesh provides a higher resolution than the computational domain needed to display the detailed behavior of a two-phase flow, the boundary length will not increase.

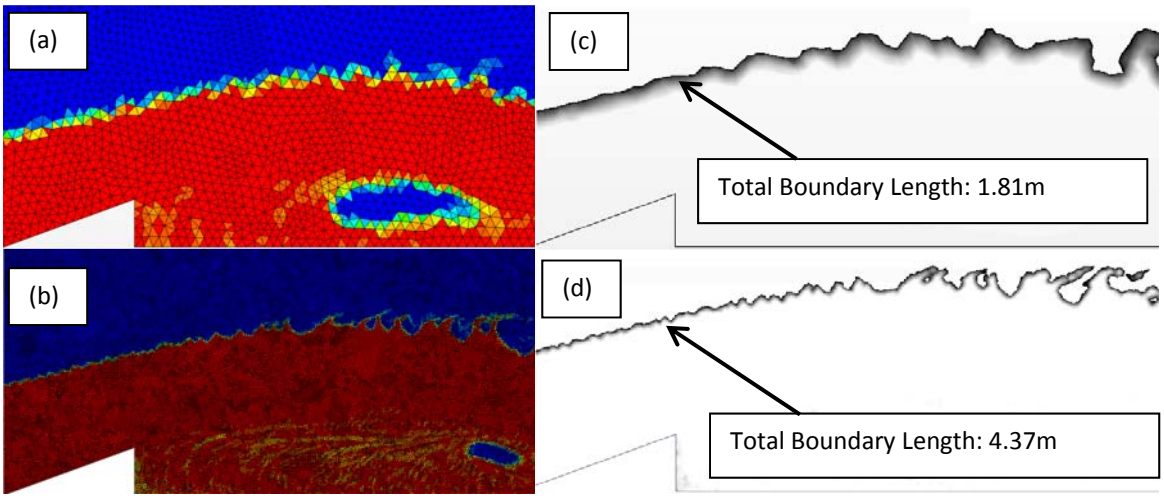

Figure 7 Comparison of 100k (a) and 1000k (b) cells

Figure 8 is the VF contour from a setup with the four different mesh sizes. Figure 8(a) is the result for 100,000 cells, and the mesh size is larger than the two-phase flow detailed waves. Only some coarse waves can be simulated, and the boundary length is 1.81m. Figure 8(b) shows the contour for the 300,000 cell mesh, which is better at simulating some details of the two-phase flow structure; the boundary length is increased to 3.54m. The results of 500,000 and 1,000,000 cell meshes are shown in Figure 8 (c) and (d), where both simulations show the similar breakup behavior of the two-phase flow; the boundary lengths are 4.62m and 4.73m, respectively.

Figure 9 summarizes the boundary lengths for the different domain cell numbers. The boundary length increases due to the better resolution of the mesh throughout the computational domain until the domain cell number reaches 500,000. However, from 500,000 to 1,000,000, the domain cell number increases 100% compared with the boundary length increase of 2%. As is clearly shown, any domain cell number higher than 500,000 is good enough to capture the breakup detail. For this reason, all the computations were made using 500,000 cells, which is considered more than enough mesh resolution to capture the smaller breakup of the liquid droplets.

Domain Cells Number	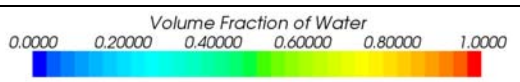	Boundary Length
100k	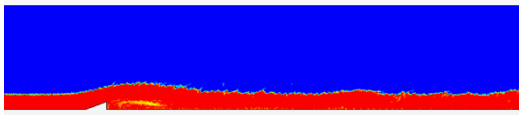	1.81m
300k	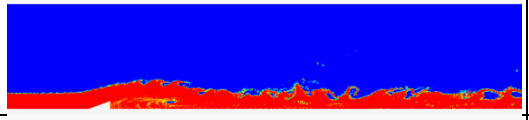	3.54m
500k	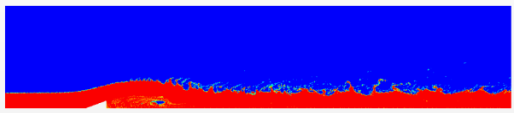	4.62m
1,000k	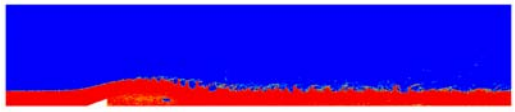	4.73m

Figure 8 VF of Water of different mesh size

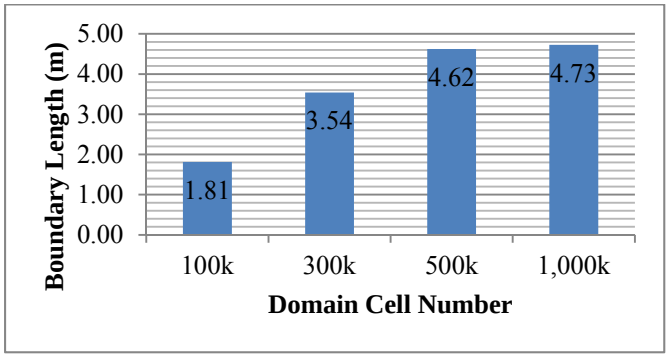

Figure 9 Boundary length of water VF for different domain cell number

Domain Cells Number	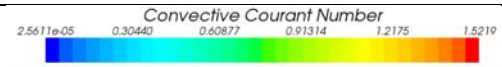
100k	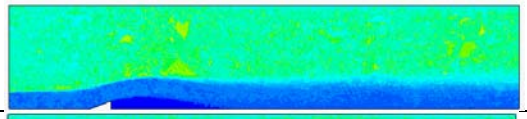
300k	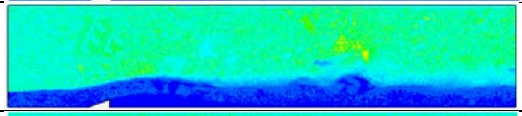
500k	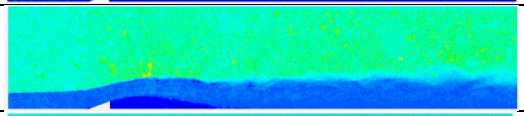
1,000k	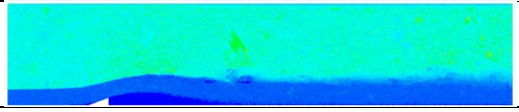

Figure 10 Courant-Friedrichs-Lewy number (CFL) for all different domain cell number

Another important reference value that needs to be checked is the Courant-Friedrichs-Lewy number (CFL), which is a dimensionless number defined in the following equation,

$$CFL = u\frac{\Delta t}{\Delta x} \quad (6)$$

where u, Δt and Δx are the fluid velocity, numerical time step, and mesh size. To maintain a CFL number of about unity (or less) is important for accuracy and to eliminate any numerical instabilities. As shown in Figure 10, this condition is satisfied over much of the flowfield and the associated computations have been verified to be stable.

VF of Water and Alumina

In this simulation, the alumina breakup behavior is compared with water, test liquid 1, liquid 2, and liquid 3. The properties of these liquids are listed in Table 2. The test liquids 1, 2 and 3 are virtual alumina with a modified surface tension and viscosity chosen to match water. In the computations of alumina and its modified test liquids, we used fluid properties corresponding to those of alumina at its melting point; however, in the simulations we set the actual temperature to 3,500K.

Table 2 VF of Water and Alumina simulation properties

Properties	Alumina	Water	Liquid 1	Liquid 2	Liquid 3
Density (kg/m3)	3,970	998	3,970	3,970	3,970
Viscosity (Pa-s)	4.6E-02	8.9E-04	4.6E-02	8.9E-04	8.9E-04
Surface Tension (N/m)	6.7E-01	7.4E-02	7.4E-02	6.7E-01	7.4E-02
Simulation Temperature (K)	3,500	300	3,500	3,500	3,500
Note			Al_2O_3 w/ surface tension of water	Al_2O_3 w/ viscosity of water	Al_2O_3 w/ both surface tension and viscosity of water

The computed VF of liquid after 2.0 sec with a 5 μsec time step and 2 inner-iterations is shown in Figure 11. Here, the air velocity and the liquid velocity are set to be constant at 26m/s and 5m/s, respectively. As shown in Figure 11, it is interesting to note that the VF behavior is different for water, alumina, and the three test liquids. Comparing the result in Figure 11, the water (a) and the alumina (b) show different flow patterns, with water film having more breakup phenomena: the boundary length is 4.20m for water but only 1.64m for the Al_2O_3 film,. We hypothesized that the different flow behaviors were due to differences in either surface tension or viscosity. To identify which factor had a more significant impact on the flow separation/recirculation, several test runs were attempted with modified fluid properties for the alumina layer. Test fluid 1, Figure 11(c), with modified alumina surface tension equivalent to the surface tension of water shows more breakup and a longer boundary length of 2.89m compared to the 1.64m boundary length of the Al_2O_3 film. The result of test liquid 2 with a modified viscosity setting is shown in Figure 11(d); the breakup phenomenon is similar to Al_2O_3 film with the boundary length of 1.71m, a much less significant change when compared with liquid 1. Finally, fluid 3, as shown in Figure 11(e), is the fluid of Al_2O_3 film with both the surface tension and the viscosity setting to be equivalent to water. By reducing both physical properties, the breakup phenomenon is seen to become stronger and the boundary length increases to 3.24m.

VF of liquid	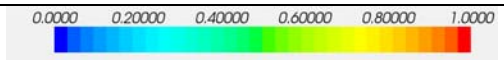	**Boundary Length**
Water film	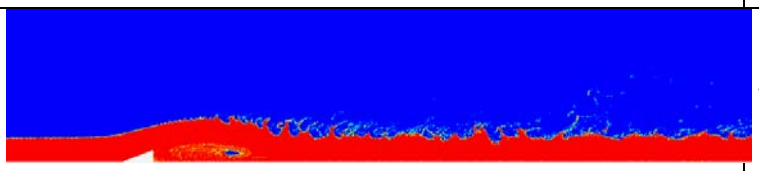	4.20m
Al_2O_3 film	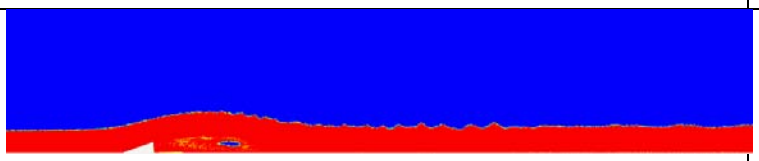	1.64m
(c) Liquid 1 Al_2O_3 w/ surface tension of water	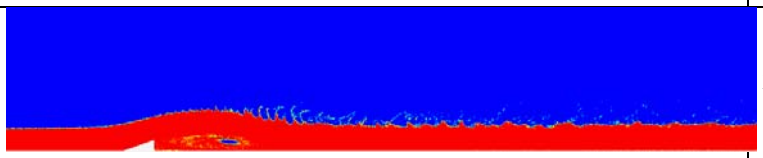	2.89m
(d) Liquid 2 Al_2O_3 w/ viscosity of water	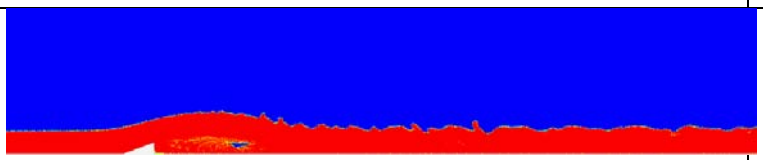	1.71m
(e) Liquid 3 Al_2O_3 w/ both surface tension and viscosity of water	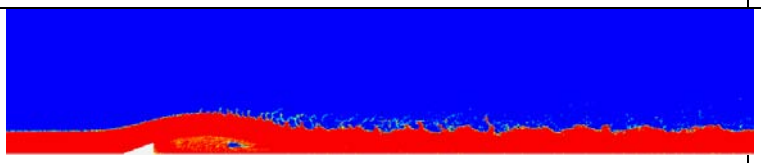	3.24m

Figure 11 VF of liquid flow. Air velocity=26m/s and liquid velocity=5m/s.

Figure 12 shows the comparison of the boundary lengths of Al_2O_3 film, liquid 1, liquid 2 and liquid 3. The boundary lengths of Al_2O_3 film, liquid 1, liquid 2, and liquid 3 are 1.64m, 2.89m, 1.71m and 3.24m, respectively, and the increases in boundary lengths over the Al_2O_3 case are 1.25m, 0.07m, and 1.60m, for liquid 1, liquid 2, and liquid 3, respectively. To investigate how surface tension affects the boundary length, we compared the case of Al_2O_3 vs. liquid 1 (case a), which showed that the boundary length increased by 76% by changing the surface tension. It could also be seen, comparing liquid 2 and liquid 3 (case b), that the boundary length of liquid 3 increased by 89% over liquid 2. In order to see the effect of viscosity affecting the boundary length, we compared the case of Al_2O_3 vs. liquid 2 (case c); the boundary length increased by 4% by changing the viscosity; also by comparing liquid 1 and liquid 3 (case d), the boundary length of liquid 3 increased by 12% over liquid 1. When comparing those two physics properties, our conclusion is that the surface tension affects the breakup behavior more significantly than the viscosity does. The relative impacts of surface tension and viscosity force are examined in more detail below when changes in the Oh number are considered.

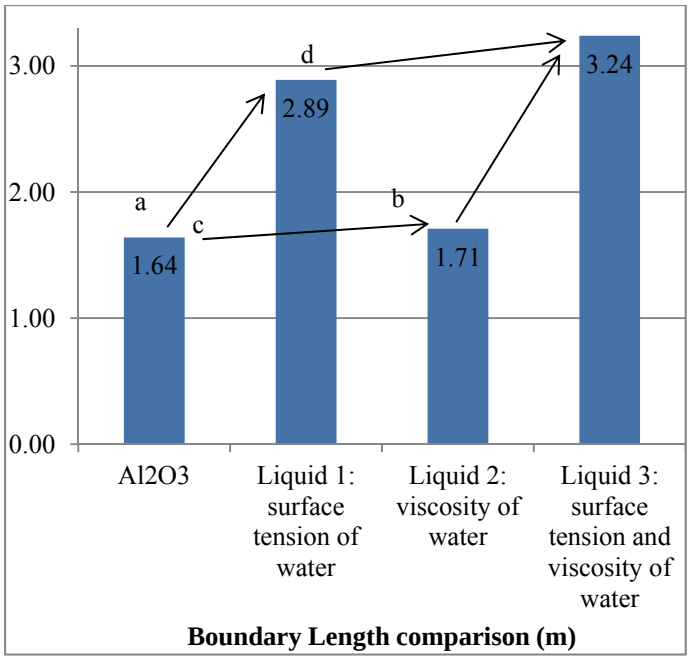

Figure 12 Boundary length comparison by surface tension and viscosity

Different Momentum Flux Ratios

The two-phase breakup mechanism strongly depends on the momentum flux ratio. Various two-phase breakup mechanisms are shown in Ishii and Grolmes[23]; the liquid disturbance can be categorized in five different patterns: roll wave, wave undercut, bubble burst, liquid impingement, and liquid bulge disintegration.

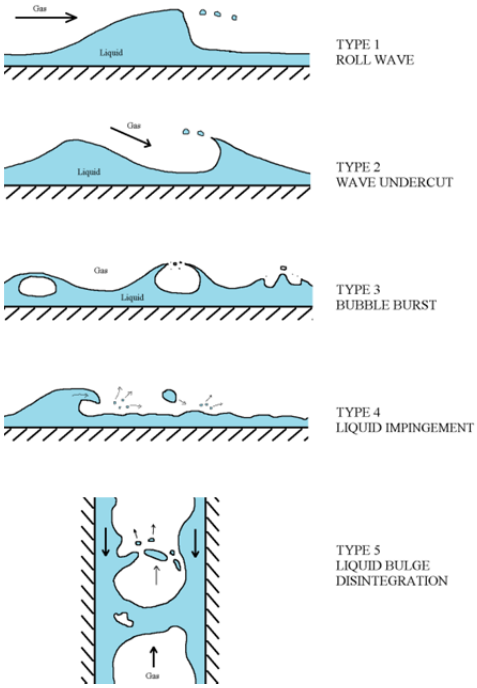

Figure 13 Various entrainment mechanisms

For the case of MFR=0.00 for alumina flow, the liquid forms into a jet type of flow pattern as seen in Figure 14 (a). This is mainly caused by the liquid momentum force; thus, the liquid penetrates into the gas region without breaking up. Figure 14 (b)-(d) shows that in the range of MFR=0.008 to MFR=0.030, the liquid film attaches to the bottom wall after passing the ramp and the waves becomes more chaotic as the MFR increases. The wave patterns shown in the cases of MFR=0.06 through MFR=0.12 fall into the category of "roll wave." In the roll wave type of entrainment, the drag force acting on the wave crests deforms the interface against the retaining force of the liquid surface tension, which results in some droplets being sheared off from the wave crest. Bubble bursting is also observed in this case, which is associated with the bursting of entrained gas bubbles. Droplets may be generated by the bubble rising to the surface of a liquid, and large droplets can also be formed by the collapse of the liquid film between the liquid film surface and the bubbles. Figure 14 (g)-(j) shows the range of MFR=0.18 to MFR=0.40. The tops of the large amplitude roll waves are sheared off from the wave crest by the gas flow and then broken into smaller droplets. Some droplets fall back into the main liquid body and then break up into smaller droplets. This latter behavior falls into the category of "liquid impingement," which is caused by relatively large liquid droplets impinging on the film interface and producing smaller droplets. An advancing roll-wave front may also produce small-size droplets by this mechanism. Wave undercuts also have been observed, caused by the undercutting of the liquid film by the gas flow. This mechanism is similar to droplet disintegration by a gas stream. The final type of entrainment, liquid bulge disintegration, is clearly shown in Figure 14 (h), (i) and (j) for a MFR=0.27 and greater, which is associated with the flooding phenomenon. When a counter-current flow reaches the flooding condition, large amplitude waves can be separated from the film to form a bulge. The bulge then disintegrates into smaller droplets due to the gas dynamics.

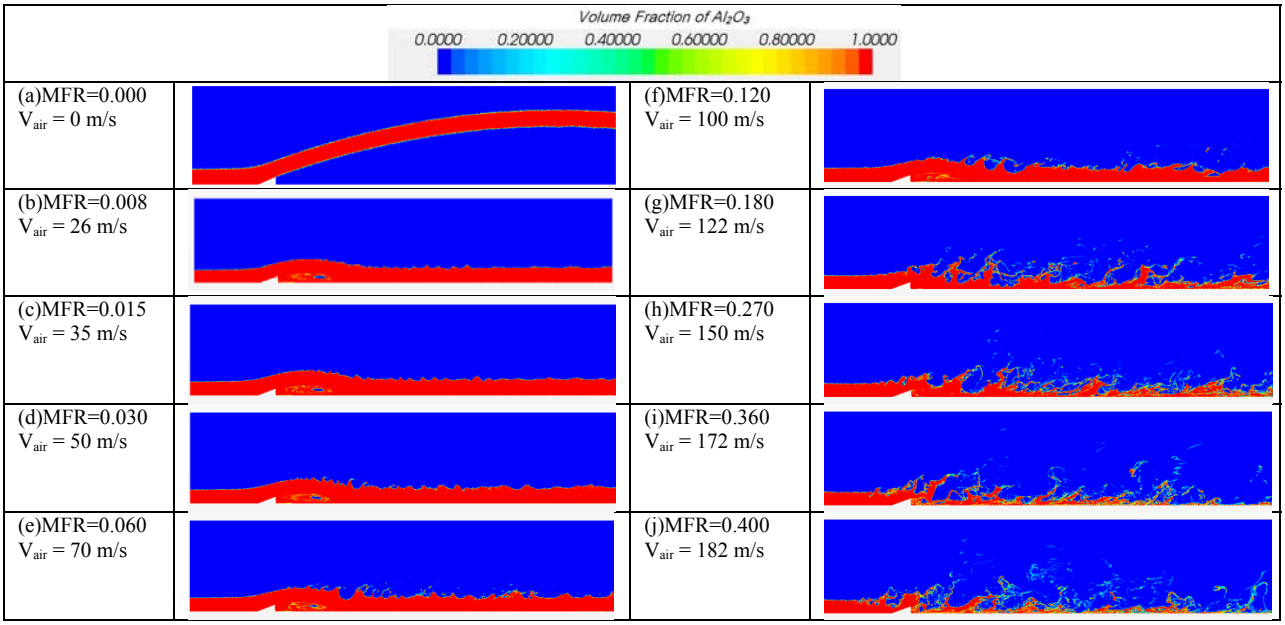

Figure 14 VF of liquid for different MFR between gas-Al2O3 streams.

Different Oh Numbers

We studied the effect of different Oh numbers by varying the physical properties in the simulations as shown in Table 3. The resulting VF contours for three different Oh number cases is shown in Figure 15. Theoretically, a large Oh number indicates a greater influence of viscosity, a damping force, compared to the surface tension force. The result should be less breakup. In this study, the Oh number is compared between water and alumina film. The simulation with Oh=6.2e-2 is controlled by changing the viscosity value of the Al_2O_3 film; the characteristic length is set up to 0.03m, which is equal to the liquid film thickness. The V_{air} and V_{liquid} are 122m/s and 5m/s, respectively, for all cases.

Table 3 physics properties setup of Oh Number simulation

	Actual Water	Actual Alumina	Alumina w/ changed viscosity
Oh	**6.0E-04**	**6.2E-03**	**6.2E-02**
μ (Pa-s)	8.9e-4	4.6E-02	4.6E-01
ρ(kg/m3)	998	2,731	2,731
σ (N/m)	0.074	0.67	0.67
L (m)	0.03	0.03	0.03

As shown in Figure 15, the bubble burst flow pattern is observed for Oh=6e-4, which is similar to the case of water. A large breakup of the wave is caused by the highly elevated roll wave motion far downstream from the ramp. For Oh=6e-3, which is the actual alumina case, more roll wave patterns appear, and a relatively small breakup of the droplets is observed. As the Oh number is raised up to 6e-2, the pattern of the waves becomes more like the "wave undercut" type of breakup. This is mainly attributed to the fact that, the viscosity is increased in order to raise the Oh number and, as a result of the large viscous forces, the gas flow can hardly penetrate into the layer and causes larger bulged waves. In addition, a lower surface tension causes a small wave breakup.

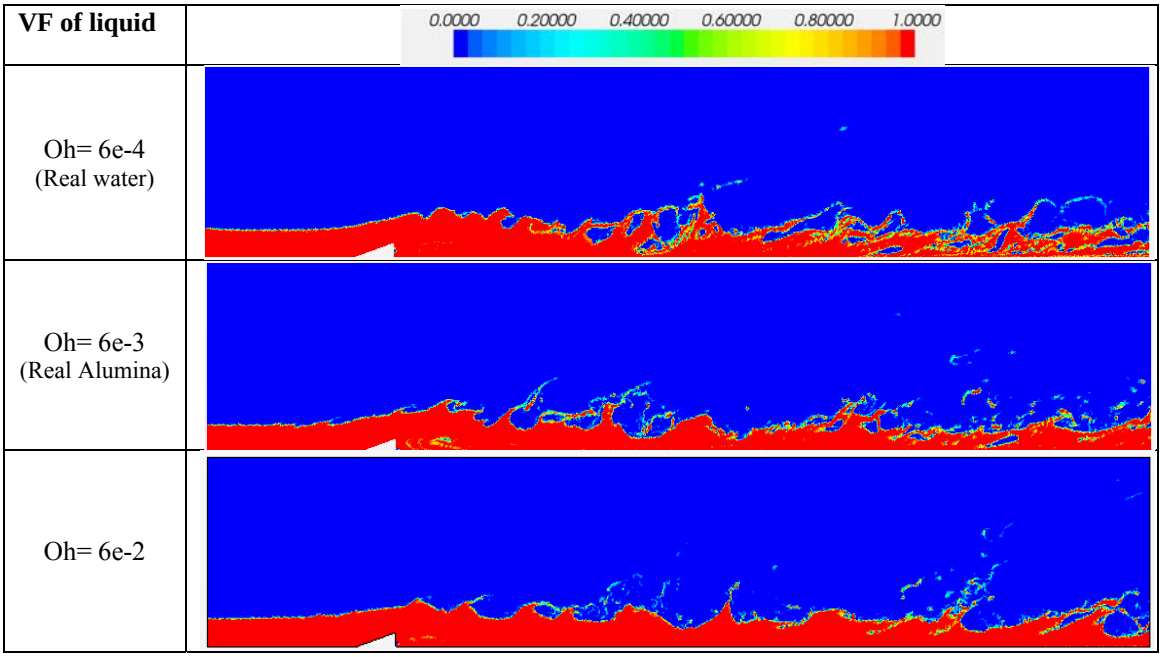

Figure 15 VF of liquid for different Oh numbers.

Volume Fraction of Liquid vs. Vorticity

The cause of the above-mentioned phenomena can be explained by comparing the Oh numbers of 6e-4 and 6e-2 with the air flow interaction. As shown in Figure 16, in the case of a lower Oh number, where surface tension effects predominates over the viscous force, the air flow and alumina interaction are governed by "roll wave" entrainment. As a result, the vorticity is relatively small and the convection of the air drags the liquid wave. The case of a large Oh number is totally different. Since the higher Oh number indicates the viscous force dominating the surface tension, a significantly higher vortex motion is generated that drives the wave into a "wave undercut" situation. As indicated by the green arrows, the large vorticity affects the generation of the wave undercut gulfs.

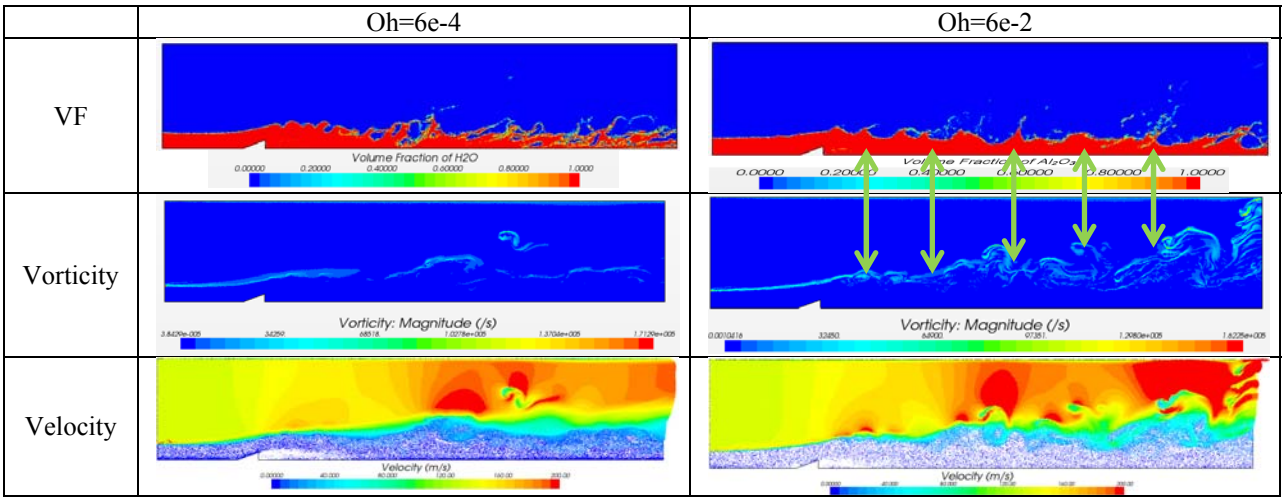

Figure 16 Comparison of VF and vorticity for Oh=6e-4 and 6e-2.

Volume Fraction of Liquid vs. Velocity

The interaction between the VF of the liquid and the velocity of air is shown in Figure 17 for different Oh number cases. As shown, the roll wave effect is clearly visualized for the smaller Oh number, and the wave undercut pattern is seen for the higher Oh number. Figure 18 shows the close-up views of the Oh=6e-4 and 6e-2. In these two figures, it is observed that for the lower Oh number cases where the surface tension is predominant over the viscous effect, more "bursting" phenomena occur, while for the higher Oh number cases the interacting flow causes more "wave undercutting" phenomena. Thus, a greater number of large-scale waves appear with higher Oh numbers.

Velocity Vector Bar	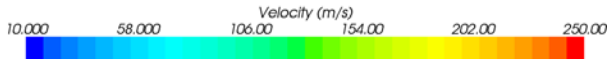
VF of Liquid	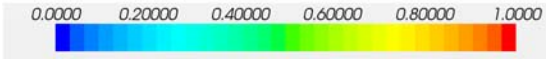
Oh= 6e-4 (Real water)	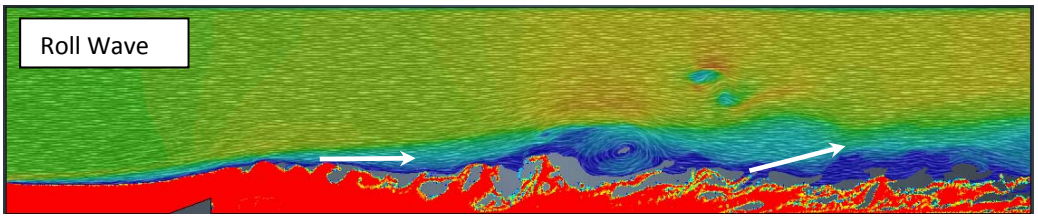
Oh= 6e-3 (Real Alumina)	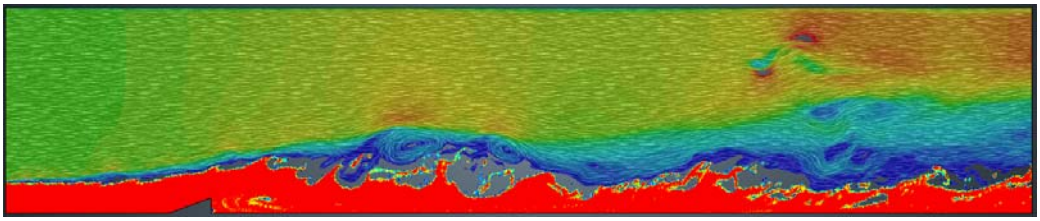
Oh= 6e-2	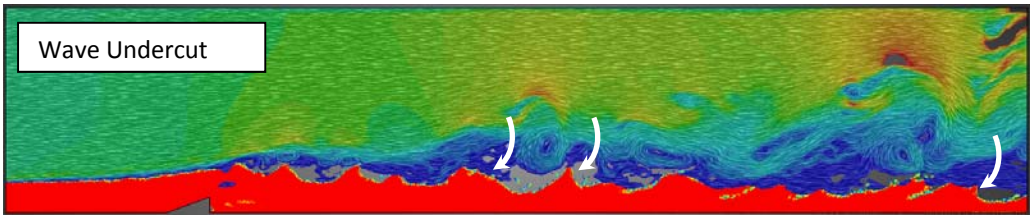

Figure 17 VF and velocity for different Oh number cases.

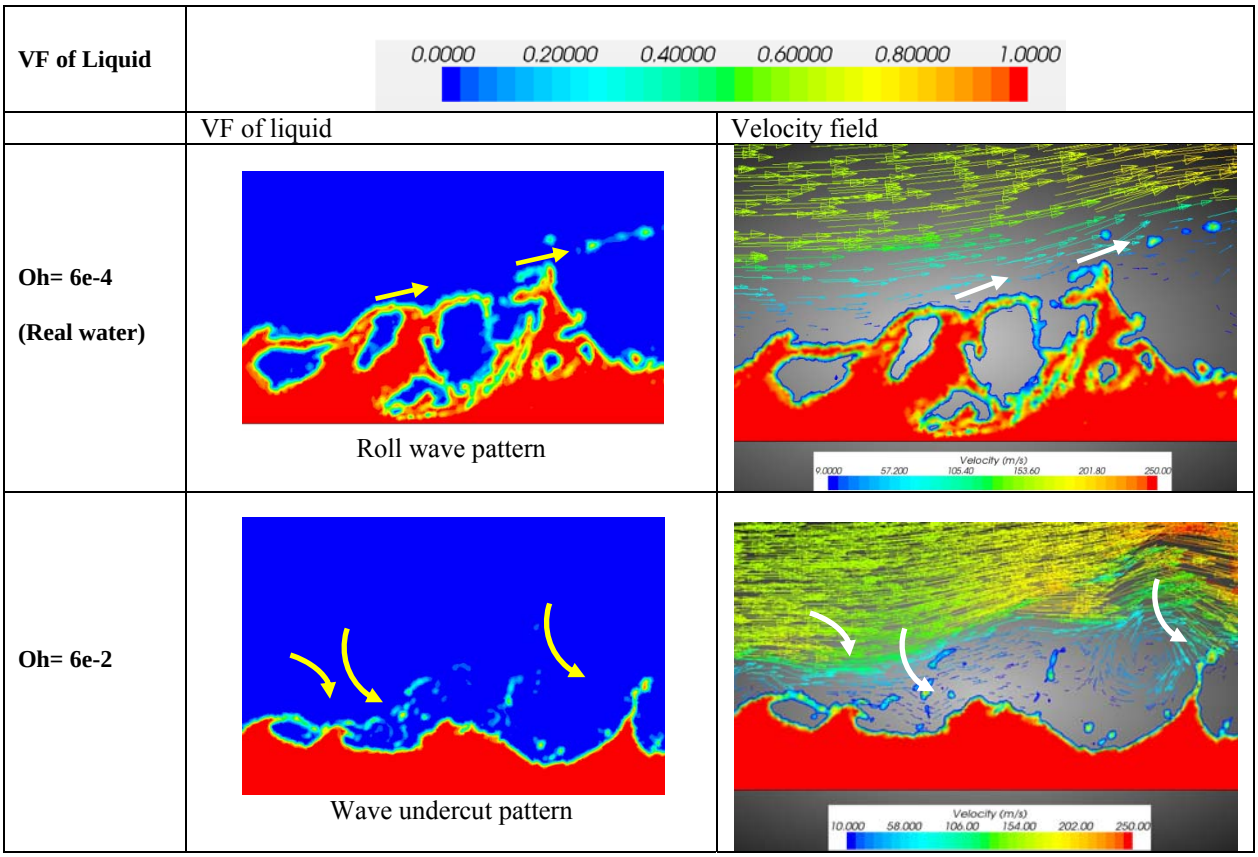

Figure 18 Close-up of VF and velocity for Oh=6e-4 and 6e-2.

Breakup Characteristic Length

By averaging the characteristic length over 0.2 sec with a time interval of 0.0002 sec (1,000 sets of VF raw data) for every MFR case, each breakup characteristic length can be easily shown, as in Figure 19. As the MFR increases, or, equivalently here, the velocity of the air increases, the boundary length increases, leading to a smaller breakup characteristic length. It is also been observed that, when MFR>0.27, the characteristic length becomes smaller and surface tension becomes a dominant factor by preventing further breakup; therefore, the decreasing trend of the characteristic length is observed to slow down. This phenomenon could also be informed by the Weber number as discussed in the following sub-section.

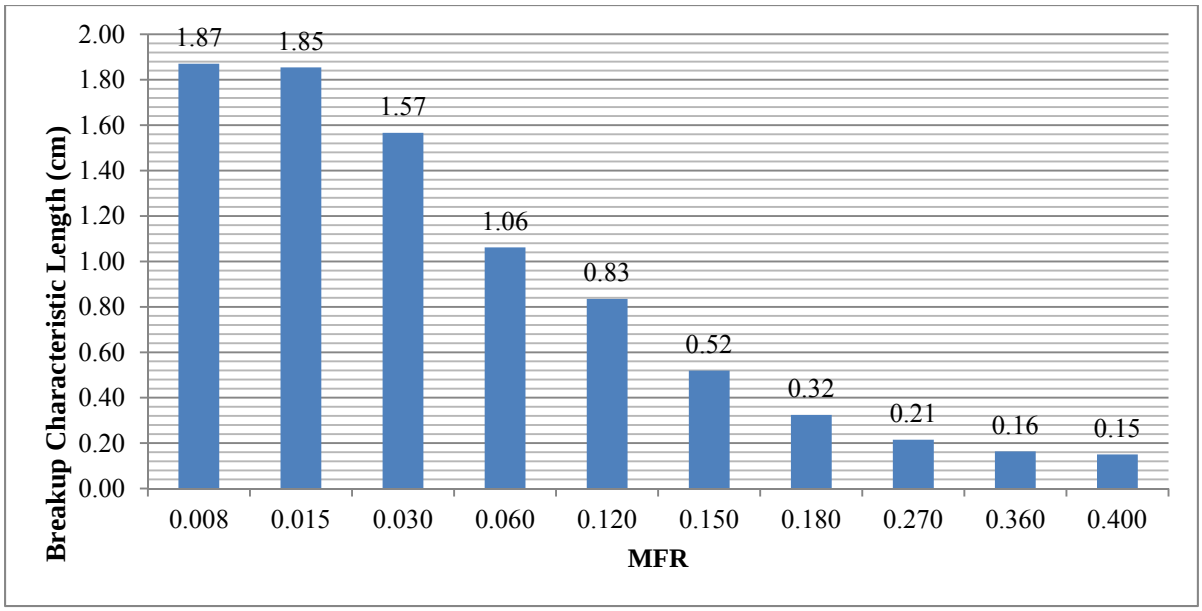

Figure 19: Breakup characteristic length for different alumina MFR settings.

Weber Number

The Weber number ($We = \rho v^2 L/\sigma$) gives the ratio of a fluid's inertia to the surface tension; a higher Weber number for a droplet indicates a higher likelihood of breakup. The Weber number is defined by density, velocity, characteristic length, and surface tension. Since density and surface tension of liquid alumina are constant, the combination of velocity and characteristic length will affect the Weber number. When the air velocity increases, the liquid characteristic length decreases. However, the relation between the velocity and the characteristic length is not a linear relation, so the Weber number should be treated carefully. The characteristic length data used for calculating Weber Number in this study are from the result shown in Figure 19.

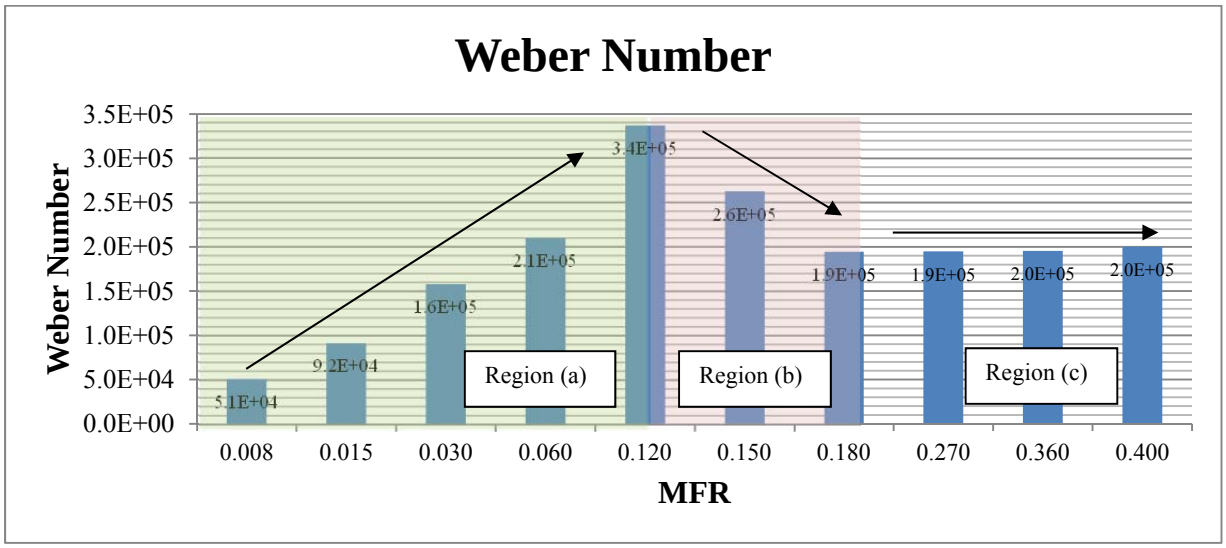

Figure 20: Weber number vs. MFR.

The Weber numbers vs. the corresponding MFR are shown in Figure 20. Since the Weber number indicates the likelihood of droplet breakup into smaller sizes, it could be observed that the likelihood of breakup for a droplet in Region (a), the MFR cases of 0.008 < MFR < 0.12 increases with MFR, until it reaches a peak value at MFR=0.12,

which gives the greatest likelihood of breakup into smaller droplet sizes. For the MFR 0.12 < MFR < 0.18 cases in Region (b), the likelihood of droplet breakup decreases from the peak at MFR=0.12, but the droplet breakup process is still ongoing. Region (c) is the MFR range of 0.18 < MFR < 0.40 where the characteristic length decreases are commensurate with air velocity increases; the result is a steady Weber number, and in this region the likelihood of breakup into smaller size droplets does not change much.

As shown in Figure 20, the breakup behavior and type of breakup events varies with MFR until a MFR threshold of 0.18 is reached. The impact of Weber number is less clear from these simulations, although the Oh discussion given previously clearly indicates that the relative value of the surface tension is important. The MFR represents a measure of the aerodynamic forces prom ting breakup, while the Weber number represents forces opposing atomization. Given that their relative magnitudes are quite disparate, i.e., the MFR is O(-3) to O(-1), while the inverse of the Weber number is several orders of magnitude smaller, i.e., O(-5), the lack of a definite correlation is not surprising.

III CONCLUSIONS

Liquid breakup processes in a co-flowing gas-liquid interface was simulated by using the Eulerian VOF method for different flow conditions and reasonable results were obtained. Importantly, the breakup boundary length and the breakup characteristic length were devised to quantify the breakup phenomenon in these studies. Grid resolution and time-step studies were also carried out to insure grid independence and overall stability of the computations. From this study, the following important conclusions emerged.

1. The momentum flux ratio (MFR) was identified as an important parameter. MFR strongly affected the flow breakup behavior – as the MFR increases, breakup boundary length increases and the breakup characteristic length decreases – the corresponding physical phenomena is the development of smaller droplets during the breakup process. In fact, as the MFR was varied in our simulations (from 0.008 to 0.4), an entire range of breakup mechanisms were observed that correspond to the mechanisms identified previously in Reference 23.

2. Our investigation of Oh number effects shows that the wave shape and breakup phenomena were impacted by the relative strength of viscous and surface tension forces. At higher Oh numbers, wider roll waves were observed, and less vorticity was produced, resulting in wave undercutting phenomena and relatively less atomization than at lower Oh numbers.

3. The Weber number increases with an increasing MFR within the range of 0.008 < MFR < 0.12 to its peak value of We=3.4E+5 and then decreases in the range of 0.12 < MFR < 0.18 to the value around We=2.0E+5 and then becomes a steady value of We≒2.0E+5in the range of 0.18 < MFR < 0.40.

IV ACKNOWLEDGMENTS

The funding for this study was supported by the U. S. Air Force Research Laboratory at Edwards Air Force Base through an AFOSR-funded Summer Faculty Fellowship Program (SFFP).

V REFERENCES

[1] Xiao, Y.M., R.S. Amano, "Aluminized composite solid propellant particle path in the combustion chamber of a solid rocket motor," *Advances in Fluid Mechanics VI, WIT Press,* 2006.
[2] D. C. Rapp, "High Energy-Density Liquid Rocket Fuel Performance," Sverdrup Technology, Inc; NASA Lewis Research Center, Brook Park, Ohio, 1968.
[3] Thakre, P., Yang, V., "Chemical Erosion of Refractory-Metal Nozzle Inserts in Solid-Propellant Rocket Motors," *J. Propulsion and Power, Vol. 25, no.1,* 2009.
[4] Wong, E. Y., "Solid Rocket Nozzle Design Summary," 4th AIAA Propulsion Joint Specialist Conference, Cleveland, OH, AIAA, Paper 68-665, 1968.

[5] Nayfeh, A. H., Saric, W. S., "Nonlinear Stability of a Liquid Film Adjacent to a Supersonic Stream," *Journal of Fluid Mechanics, Vol. 58,* pp. 39-51, 1973.
[6] S. Borass, "Modeling Slag Deposition in the Space Shuttle Solid Rocket Motor," *Journal of Spacecraft and Rockets. Vol 21,* pp. 47-54, 1984.
[7] M. Salita, "Deficiencies and Requirements in Modeling of Slag Generation in Solid Rocket Motors," *Journal of Propulsion and Power, Vol.11,* pp. 10-23, 1995.
[8] Hess, E., Chen, K., Acosta, P., Brent, D., Fendell, F.; "Effect of Aluminized-Grain Design on Slag Accumulation," *Journal of Spacecraft and Rockets, Vol. 29,* pp. 697-703, 1992.
[9] Xiao, Y., Amano, R. S., Cai, T., Li, J, "A New Method to Determine the Velocities of Particles on a Solid-Propellant Surface," *ASME Journal of Heat Transfer, Vol. 127,* pp. 1057-1061, 2005.
[10] Xiao, Yumin, Amano, R.S., Cai, T., and Li, J., "Particle Velocity on Solid-Propellant Surface Using X-Ray Real Time Radiography," *AIAA Journal, Vol. 41, No. 9,* pp. 1763-1770, September 2003.
[11] Bandera, A., Maggi, F., and Deluca, L.T., "Agglomeration of Aluminized Solid Rocket Propellants," in *45th AIAA/ASME/SAE/ASEE Joint Propulsion Conference & Exhibit*, Denver, Colorado.
[12] R. Holtzmann, "Introduction-The Nature of an Advanced Propellant," Aerojet-General Corporation Von Karman Center, [Online]. Available: web.anl.gov/PCS/acsfuel/preprint%20archive/Files/Volumes/Vol09-1.pdf.
[13] Hinze, J.O., "Fundamentals of the Hydrodynamic Mechanism of Splitting in Dispersion Processes," *A.I.Ch.E. Journal*, Vol. 1, No. 3, 1955, pp. 289-295.
[14] Hinze, J.O., "Critical Speeds and Sizes of Liquid Globules," *Applied Scientific Research, A1*, 1949, pp. 273-288
[15] Mark Salita. "Deficiencies and requirements in modeling of slag generation in solid rocket motors", Journal of Propulsion and Power, Vol. 11, No. 1 (1995), pp. 10-23.
[16] CD-adapco, [Online]. Available: http://www.cd-adapco.com/products/star-ccm-plus.
[17] Hirt, C.W., Nichols, B.D., "Volume of fluid (VOF) method for the dynamics of free boundaries," *Journal of Computational Physics 39 (1),* pp. 201-225, 1981.
[18] B. E. Launder, G.J.Reece, W. Rodi, *Progress in the development of a Reynolds-stress turbulence closure.* J. Fluid Mech, 1974. 68(3): p. 537-566.
[19] Young, Albert C., Omatete, Ogbemi O., Janney, Mark A., Menchhofer, Paul A., "Gelcasting of Alumina," *J. Am. Ceram. Soc. 74[3],* pp. 612-618, 1991.
[20] Blomquist , B. A., Fink, J. K., Leibowitz, L., "The Viscosity of Molten Alumina," Argonne National Laboratory, Argonne, IL, 1978.
[21] Glorieux, B., Millot, F., Rifflet, J. C., "Surface Tension of Liquid Alumina from Contactless Techniques," *Internaional Journal of Thermophysics,* pp. 1249-1257, 2002.
[22] Glorieux, B., Millot, F., Rifflet, J.-C., Coutures, J.-P., "Density of Superheated and Undercooled Liquid Alumina by a Contactless Method," *International Journal of Thermophysics,* pp. 1085-1094, 1999.
[23] Ishii, M. and Grolmes, M.A., "Inception criteria for droplet entrainment in two-phase concurrent film flow," *AIChE Journal, Volume 21, Issue 2,* pp. 308-318, March 1975.